Research Square

Preprints are preliminary reports that have not undergone peer review. They should not be considered conclusive, used to inform clinical practice, or referenced by the media as validated information.

Distributed Stability-Constrained Operation of Receiving-End Grids with Multiple Operators and High-Voltage Direct-Current Infeeds

Xiaobo Wang

xiaobo.wang@sjtu.edu.cn

State Grid Jiangsu Electric Power Research Institute

Haifeng Li

State Grid Jiangsu Electric Power (China)Power Dispatching and Control Center, State Grid Jiangsu Electric Power Co.

Zhe Chen

State Grid Jiangsu Electric Power Research Institute

Tao Jin

State Grid Jiangsu Electric Power (China)Power Dispatching and Control Center, State Grid Jiangsu Electric Power Co.

Mingshen Wang

State Grid Jiangsu Electric Power Research Institute

Article

Keywords:

Posted Date: October 23rd, 2026

DOI: https://doi.org/10.21203/rs.3.rs-11215044/v1

License: This work is licensed under a Creative Commons Attribution 4.0 International License. Read Full License

Additional Declarations: No competing interests reported.

Distributed Stability-Constrained Operation of Receiving-End Grids with Multiple Operators and High-Voltage Direct-Current Infeeds

Xiaobo Wang[1,3*], Haifeng Li[2], Zhe Chen[1], Tao Jin[2], Mingshen Wang[1]

[1*]State Grid Jiangsu Electric Power Research Institute, Nanjing, 211103, China.
[2]Power Dispatching and Control Center, State Grid Jiangsu Electric Power Co., Ltd., Nanjing, 210024, China.
[3]School of Electrical Engineering, Shanghai Jiao Tong University, Shanghai, 200240, China.

*Corresponding author(s). E-mail(s): xiaobo.wang@sjtu.edu.cn;

Abstract

Coupling between active and reactive power at high-voltage direct-current (HVDC) infeed buses and inconsistent decisions among multiple operators increase the instability risk of receiving-end grids. To address this problem, this paper proposes a distributed stability-constrained operation method for receiving-end grids with multiple operators and HVDC infeeds. A reduced-order alternating-current/direct-current dynamic model is formulated to capture the coupling between active and reactive power. A Lyapunov stability index is then formulated from the state-space model to evaluate the stability of the receiving-end grid. An adaptive cutting-plane algorithm embeds this implicit index in optimal power flow by generating corrective cuts through posterior operating-point verification. A selection-matrix-based consensus form of the alternating direction method of multipliers (ADMM) is developed to coordinate regional generation and HVDC transfers owned by different operators without sharing complete private objective functions or internal scheduling records. Simulation results on a 24-hour receiving-end-grid case constructed from the IEEE 39-bus benchmark show that the proposed method obtains optimal operating decisions for the receiving-end grid, reduces the hourly stability-violation rate by 12.5%, and increases operating cost by only 0.12%.

Keywords: multiple-operator receiving-end grid, HVDC infeed, small-disturbance stability, adaptive stability cuts, selection-matrix-based consensus ADMM

Nomenclature

Symbol	Description
Abbreviations	
AC/DC	Alternating-current/direct-current coupling at an HVDC terminal.
ADMM	Alternating direction method of multipliers.
HVDC	High-voltage direct current.
MVA/MVAr	Megavolt-ampere/megavolt-ampere reactive.
MW/MWh	Megawatt/megawatt-hour.
OPF	Optimal power flow.
P–Q	Active–reactive power coupling.
P–f/Q–V	Active-power–frequency/reactive-power–voltage control.
p.u.	Per unit.
RES	Renewable energy source.
SDP	Semidefinite programming.
Sets and indices	
$\mathcal{N}, \mathcal{L}$	Sets of buses and transmission branches.
$\mathcal{G}, \mathcal{D}$	Sets of dispatchable injections and receiving-end HVDC terminals, $\mathcal{D} \subseteq \mathcal{G}$.
$\mathcal{R}, \mathcal{T}$	Sets of regional operators and hourly operating periods.
$\mathcal{N}_r, \mathcal{D}_r, \mathcal{G}_r$	Buses, HVDC terminals, and dispatchable units owned by operator r.
$\mathcal{G}_i$	Units connected to bus i.
$\mathcal{C}_t$	Set of accumulated stability cuts for period t.
i, j, e, g, r, t	Indices of buses, adjacent buses, branches, units, operators, and periods.
k, q	Inner ADMM iteration and outer stability-cut iteration.
$\lvert\mathcal{G}\rvert$	Number of dispatchable units.
Network, resource, and cost parameters	
B_{base}	System power base.
$x_{ij}, a_{ij}, \varphi_{ij}$	Reactance, transformer tap ratio, and phase shift of branch (i, j).
ν_{ij}, b_{ij}	Branch status and tap-adjusted DC susceptance of branch (i, j).
G_{ij}, B_{ij}	Real and imaginary entries of the AC bus-admittance matrix.
σ_{ie}	Signed bus–branch incidence coefficient, positive at the from bus.
$\overline{F}_{ij}, \overline{S}_{ij}$	Adopted active-transfer and apparent-power limits of branch (i, j).
$P_g^{\min}, P_g^{\max}$	Minimum and nameplate maximum active power of unit g.
S_d^{rated}	Rated apparent power of receiving-end HVDC terminal d.

κ_d	Active–reactive terminal coupling coefficient of HVDC infeed d.
$\widehat{P}_d^{\max}$	Effective HVDC active-transfer bound after reactive-power occupation.
α	Minimum dynamic-support output factor.
c_d^P, c_d^Q, c_d^S	HVDC active-transfer, reactive-exchange, and apparent-capacity cost coefficients.
$c_0^{(2)}, c_0^{(1)}$	Quadratic and linear external-grid cost coefficients.
$P_{i,t}^{\mathrm{L}}, P_{i,t}^{\mathrm{RES}}$	Active load and renewable injection at bus i.
$Q_{i,t}^{\mathrm{L}}, P_{i,t}^{\mathrm{G}}, Q_{i,t}^{\mathrm{G}}$	Reactive load and aggregate AC active/reactive generation at bus i.

Dynamic and stability parameters

$m_{P,d}^0, m_{Q,d}^0$	Nominal active- and reactive-channel terminal control coefficients.
$\tau_{P,d}^0, \tau_{V,d}^0$	Nominal active-power filter and voltage-response time constants.
$M_{P,t}, M_{Q,t}, T_{P,t}, T_{V,t}$	Diagonal operating-point terminal parameter matrices.
K_{QP}	Diagonal incremental HVDC active–reactive coupling matrix.
γ_J	Scaling coefficient of the scheduling network Jacobian.
ϵ	Positive-definiteness lower bound for the Lyapunov matrix.
$\bar{\eta}^{\mathrm{M}}$	SDP target used by the scheduling master problem.
$\bar{\alpha}, \epsilon_\alpha$	Required AC spectral abscissa and its numerical acceptance tolerance.
$\epsilon_\eta, \varepsilon_C$	SDP numerical tolerance and AC-projection economic tie-break weight.
$\Delta P, \boldsymbol{e}_g$	Finite-difference perturbation and unit vector associated with unit g.

Operational variables and functions

$P_{d,t}^{dc}, Q_{d,t}^{dc}, S_{d,t}^{dc}$	Active, reactive, and apparent terminal power of HVDC infeed d.
$P_{g,t}$	Active injection of dispatchable unit or terminal g.
$P_{0,t}$	Active power exchanged with the external-grid equivalent.
$V_{i,t}, \theta_{i,t}$	AC bus-voltage magnitude and angle.
$Y = G + \mathrm{j}B, \theta_{ij,t}$	Bus-admittance matrix and voltage-angle difference $\theta_{i,t} - \theta_{j,t}$.
$F_{ij,t}, P_{ij,t}, Q_{ij,t}$	Master active transfer and AC active/reactive branch flows.
$\ell_{d,t}^{dc}, \ell_{d,t}^P$	Full P–Q and active-only loading ratios of HVDC terminal d.
$C_t^P, C_t^Q, C_t^S, C_t^{\mathrm{grid}}$	Active, reactive, capacity-occupation, and external-grid cost components.
C_t, C	Period operating cost and total multi-period cost.
$\widetilde{\boldsymbol{P}}_t, \boldsymbol{P}_t^{\mathrm{AC}}$	Convex-master dispatch and final AC-projected dispatch.
$\boldsymbol{Q}_t^{\mathrm{AC}}, \boldsymbol{V}_t^{\mathrm{AC}}, \boldsymbol{\theta}_t^{\mathrm{AC}}$	AC-projected reactive dispatch, voltage magnitudes, and angles.
$C_{r,t}, \boldsymbol{P}_{r,t}$	Local operating cost and owned dispatch vector of operator r in period t.
$\underline{\boldsymbol{P}}_r, \overline{\boldsymbol{P}}_r$	Operator-owned vectors of lower and upper dispatch bounds.

Dynamic matrices and stability quantities

$\Delta\boldsymbol{\delta}_t, \Delta\boldsymbol{V}_t$	Retained terminal-angle and voltage deviations.

$\Delta \boldsymbol{p}_{m,t}, \Delta \boldsymbol{v}_t^a$	Measured active-power and actuator-output deviations in the validation model.
A_t^V, A_t^{AC}	Scheduling and independent validation voltage-dynamic state matrices.
$J_{P\theta,t}, J_{PV,t}$	Reduced active-power sensitivities to terminal angle and voltage.
$J_{Q\theta,t}, J_{QV,t}$	Reduced reactive-power sensitivities to terminal angle and voltage.
$J_{\mathrm{red},t}, J_{\mathrm{red},t}^{\mathrm{AC}}$	Scheduling and operating-point reduced P/Q–angle/voltage Jacobians.
T^a, τ_g^a	Actuator-lag matrix and actuator time constant.
$J_{dd,t}^{\mathrm{AC}}, J_{da,t}^{\mathrm{AC}}$	Dynamic–dynamic and dynamic–algebraic blocks of the grounded AC Jacobian.
$J_{ad,t}^{\mathrm{AC}}, J_{aa,t}^{\mathrm{AC}}$	Algebraic–dynamic and algebraic–algebraic blocks of the grounded AC Jacobian.
$\lambda, \alpha_t^{\mathrm{AC}}$	Eigenvalue and spectral abscissa of the AC-Jacobian validation model.
Φ_t, I	Lyapunov matrix and identity matrix of compatible dimension.
$\eta_t(\boldsymbol{P}_t^{dc}, \boldsymbol{Q}_t^{dc}), \eta_t^{\mathrm{re}}$	Scheduling SDP index and its value re-evaluated at the candidate dispatch.
$\nabla \eta_t^{(q)}, \nabla \alpha_t^{(q)}$	Master-dispatch sensitivities of the SDP index and validation spectral abscissa.
$\mathrm{diag}(\cdot)$	Operator that forms a diagonal matrix from its arguments.
$\mathrm{sym}(X)$	Symmetric part $(X + X^\top)/2$ of matrix X.
$\mathrm{clip}_{[a,b]}(x)$	Projection of scalar x onto the interval $[a, b]$.
Distributed-solution quantities	
$\Omega_t^{\mathrm{M}}, \Omega_t^{\mathrm{AC}}, \Omega_t^{\mathrm{stab}}$	Convex-master, nonlinear network-feasibility, and accumulated stability-cut sets.
E_r	Selection matrix mapping system dispatch to units owned by operator r.
$\boldsymbol{x}_{r,t}, \boldsymbol{z}_t, \boldsymbol{u}_{r,t}$	Operator dispatch proposal, system consensus dispatch, and scaled dual variable.
$\boldsymbol{x}_r, \boldsymbol{z}$	Temporary operator and system decision variables in the ADMM subproblems.
$\rho_P, \epsilon_{\mathrm{ADMM}}$	Penalty and residual tolerance for the selection-matrix-based consensus ADMM.
r_t^k, s_t^k	Normalized primal and dual residuals at ADMM iteration k.

1 Introduction

Large-scale renewable resources are often concentrated far from major load centers, creating a growing need for long-distance and high-capacity transmission. High-voltage direct-current (HVDC) transmission is well suited to this role [1]. As multiple HVDC links converge on the same receiving-end grid, limited alternating-current (AC) system strength can intensify interactions between converter controls and the network. The resulting disturbance response depends on the operating point, network strength, and control interactions [2, 3]. Converter-dominated systems make this dependence more

pronounced because reduced inertia and converter controls reshape critical dynamic modes [4, 5]. Reviews of inverter-based and microgrid stability report a similar sensitivity to network support and controller settings [6, 7]. Under such conditions, a schedule may satisfy steady-state voltage and branch limits yet provide insufficient damping after a small disturbance. Ensuring voltage-dynamic security is therefore essential to the effective use of HVDC transmission capacity.

This setting calls for a scheduling framework that balances economic performance with voltage-dynamic security. At its core, the framework must coordinate HVDC transfers and local generation so that the resulting AC operating point satisfies both network constraints and a prescribed dynamic margin. It should also avoid overly conservative transfer limits that leave available HVDC capacity unused. If different operators own the participating terminals and resources, their decisions must be coordinated across regional boundaries. The resulting problem thus links economic dispatch, operating-point stability assessment, and multi-operator coordination.

A key challenge is to capture how dispatch decisions affect the stability margin. Under the terminal P–Q characteristic adopted in this study, adjustments to HVDC active power also change reactive-power exchange and apparent-power loading. These changes reshape the voltage profile and the power-flow Jacobian, thereby modifying terminal-control interactions and linearized voltage dynamics. Because multiple infeeds interact through the shared AC network, their effects must be evaluated at a common operating point. Multi-infeed system-strength indices can identify weak AC support and converter interactions [8]. However, they do not indicate how individual terminals should be redispatched to meet the voltage-dynamic limit. Likewise, enforcing the P–Q relation in steady-state optimal power flow (OPF) does not ensure that an active-power-only dynamic model represents the corresponding incremental reactive response. A suitable dispatch model must therefore retain this response in the stability assessment.

Another challenge is to embed an operating-point-dependent stability limit in the optimization. Stability-constrained scheduling links security requirements with economic decisions [9]. Earlier formulations incorporated transient or small-signal security into OPF through time-domain simulation, eigenvalue sensitivities, and sequential quadratic programming [10–12]. More recent methods use model-based convexification [13], stability-margin sensitivities [14], or learned stability boundaries [15]. Lyapunov inequalities and semidefinite programming (SDP) provide a further model-based approach [16, 17]. At a given operating point, the sensitivity of an SDP index can yield an affine constraint on dispatch [18, 19]. The resulting constraint, however, is only a local approximation. Economic redispatch followed by nonlinear AC projection may alter reactive-power balance, bus voltages, network losses, and the dynamic state matrix. Consequently, a candidate may satisfy the affine constraint but fail the final dynamic check. The optimization therefore requires repeated operating-point evaluation and corrective constraints after failed checks.

A further challenge arises from coordination among regional operators. Their schedules jointly determine tie-line flows and the stability margin of the interconnected grid. Distributed OPF commonly employs decomposition and the alternating direction method of multipliers (ADMM) to coordinate network-coupled decisions [20–23]. Distributed small-disturbance assessment has also been studied for inverter-based

microgrids [24]. In the setting considered here, the corrective stability constraints act on active-power outputs, whereas final verification depends on the whole-grid AC operating point. Consensus on duplicated boundary states alone cannot enforce these dispatch-dependent constraints. The coordination variables must therefore connect regional active-power decisions to a shared network and stability model while allowing complete regional cost functions to remain local.

To address these challenges, this paper develops a coordinator-assisted method for stability-constrained operation. The main contributions are summarized as follows.

1. A reduced-order AC/DC voltage-dynamic model maps joint dispatch to a Lyapunov–SDP stability index. The model captures HVDC active–reactive coupling, loading-dependent controls, and the AC-network Jacobian.
2. An adaptive cutting-plane procedure re-evaluates the stability index at each candidate from the master problem. A separate higher-order AC-Jacobian model verifies the AC-projected operating point, and each violation produces a corrective cut for the next optimization cycle.
3. A selection-matrix-based consensus ADMM coordinates active-power decisions across operators. A system-level coordinator enforces shared network limits and accumulated stability cuts without collecting complete regional cost functions.

The remainder of this paper is organized as follows. Section 2 presents the overall framework and workflow of the proposed method. Section 3 develops the AC/DC voltage-dynamic model, the adaptive cutting-plane procedure, and the distributed coordination algorithm. Section 4 describes the test system and evaluates the proposed method through numerical studies. Section 5 summarizes the main findings and concludes the paper.

2 Multi-Operator Architecture and Distributed Solution Workflow

2.1 Multi-operator coordination architecture

The study considers a receiving-end grid supplied by several aggregated HVDC terminals and operated by multiple regional operators. Each operator manages a regional subnetwork, its local resources, and a subset of HVDC infeeds. The regions remain electrically coupled through inter-operator tie lines and must satisfy a common network and small-disturbance stability boundary. Their operating decisions therefore cannot be optimized independently even though their complete cost functions and internal scheduling records remain local.

Figure 1 illustrates the generic coordinator-assisted architecture for N regional operators. Each operator solves a local OPF with the applicable stability constraints and sends only its proposed schedule and selected coordination variables to the coordinator. The coordinator returns consensus signals that align the regional decisions with inter-regional power balance, shared network limits, and the system-level stability cuts. The arrows distinguish upward local proposals from downward coordination signals; they do not represent the transfer of complete regional models or objective functions.

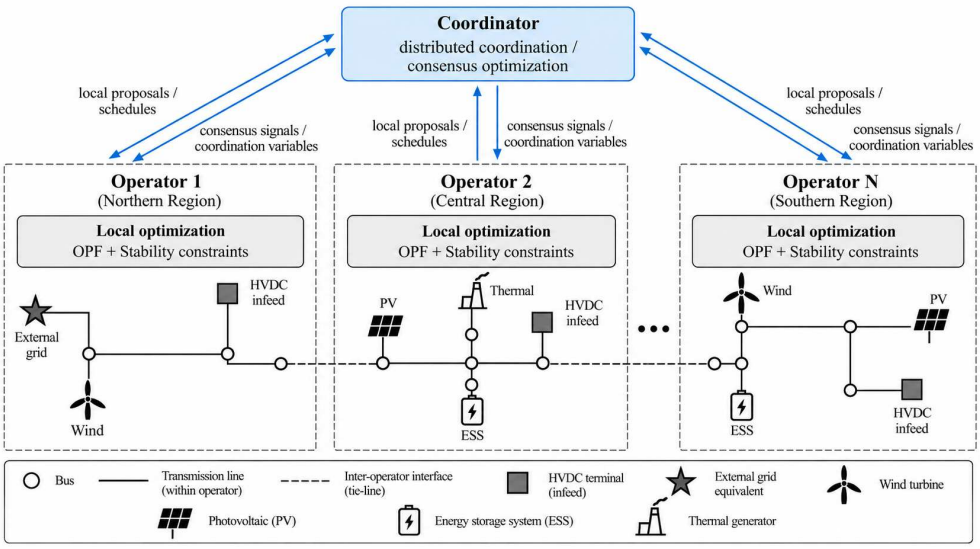

Fig. 1 Generic coordination architecture of a multiple-operator receiving-end grid. Regional operators retain their local optimization models and exchange selected schedules and coordination variables with a system-level coordinator. Solid lines denote intra-region connections, and dashed lines denote inter-operator tie lines.

The resource symbols in Fig. 1, including the energy-storage symbol, illustrate assets that a regional model may contain. Storage scheduling and unit commitment are not modeled in Section 3. The exact controllable injections, HVDC-terminal allocation, renewable locations, and operator ownership used in the numerical study are specified in Section 4.1. For the present formulation, local optimization covers the dispatch variables owned by each operator, while the coordinator handles quantities coupled by the interconnected network and accumulated stability cuts.

2.2 Distributed optimization and posterior-verification workflow

Figure 2 presents the complete computational workflow. The input layer contains regional costs and operating limits, the shared network model, the stability threshold, and the current cut set. With a fixed cut set, all operators solve their private subproblems in parallel and submit local dispatch proposals. The coordinator then applies the selection matrices, forms the active-power consensus dispatch, and enforces the shared network constraints together with all accumulated stability cuts.

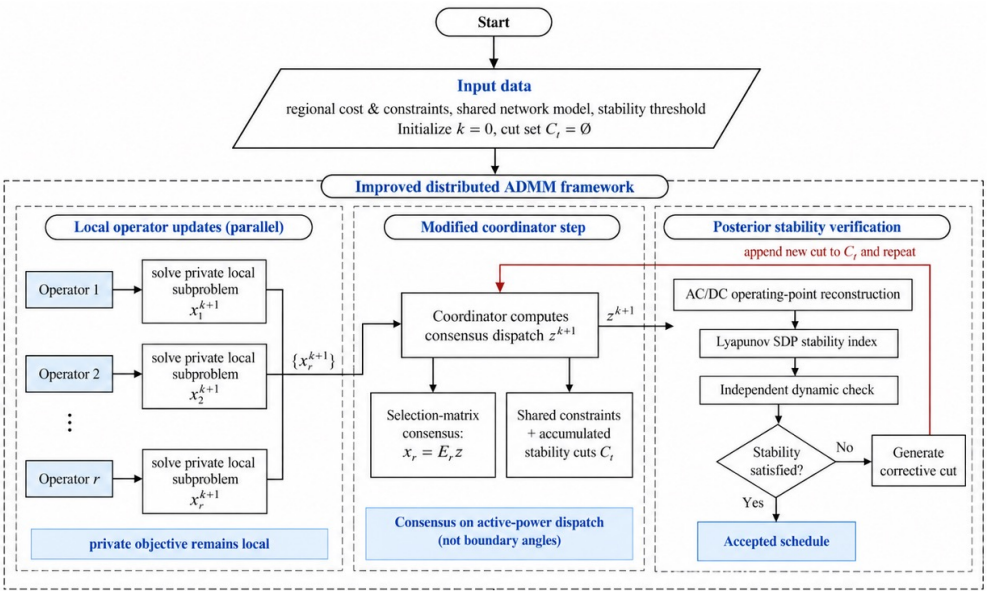

Fig. 2 Workflow of the proposed distributed stability-constrained operation method. Parallel regional updates are coordinated through active-power consensus, after which the reconstructed AC/DC operating point is verified. A failed stability check generates a corrective cut and restarts the coordinated optimization.

The coordinated dispatch is not accepted from the affine constraints alone. It is first reconstructed as a nonlinear AC/DC operating point. The resulting voltages, angles, reactive exchanges, and branch flows are used to evaluate the Lyapunov SDP index and an independent dynamic check. A candidate that passes both checks becomes the accepted schedule. Otherwise, a local sensitivity at the rejected operating point generates a corrective affine cut. The cut is appended to $\mathcal{C}_t$, and the distributed optimization is repeated. In Fig. 2, k indexes the inner ADMM iterations; adding a corrective cut starts a new outer verification cycle.

2.3 Coupling among operation, stability, and coordination

The need for the outer verification cycle follows from the operating-point dependence of the dynamic model. A change in HVDC active transfer changes terminal reactive exchange and apparent-power loading. It also changes the nonlinear AC operating point, the reduced network Jacobian, and the dynamic state matrix. The stability index is therefore a function of the coordinated dispatch rather than a fixed network attribute. Local affine cuts make this implicit relation tractable, while posterior reconstruction checks whether each candidate remains within the reliable neighborhood of those approximations.

The three methodological components have distinct roles in this workflow. The AC/DC-coupled model maps regional and HVDC dispatch decisions to the receiving-end dynamic state matrix. The adaptive cutting-plane procedure converts failed

operating-point checks into cumulative scheduling constraints. Selection-matrix-based consensus ADMM coordinates the resulting problem without pooling complete local objective functions. Together, these components produce a schedule that is economically coordinated, network feasible, and verified against the prescribed small-disturbance criterion.

The case studies follow the same sequence. The first comparison removes the incremental HVDC active–reactive coupling from the dynamic representation. The second replaces cumulative posterior correction with a single-cut approximation. The third compares distributed coordination with the centralized reference and tests the selection of active-power dispatch as the consensus variable. Each comparison therefore evaluates one specific block in Figs. 1 and 2.

3 Mathematical Formulation of Distributed Stability-Constrained Operation

This section formulates the three components introduced in Section 2: the AC/DC-coupled operation model, the adaptive stability constraints, and the selection-matrix-based consensus ADMM solution. The centralized and distributed implementations use the same physical constraints and verified stability-cut set.

3.1 AC/DC-coupled operational formulation

For each period $t \in \mathcal{T}$, the operation model minimizes HVDC active-transfer, terminal reactive-exchange, converter-capacity, and external-grid costs:

$$\min\ C = \sum_{t\in\mathcal{T}} \left(C_t^P + C_t^Q + C_t^S + C_t^{\text{grid}} \right), \tag{1}$$

where

$$C_t^P = \sum_{d\in\mathcal{D}} c_d^P (P_{d,t}^{dc})^2, \tag{2}$$

$$C_t^Q = \sum_{d\in\mathcal{D}} c_d^Q (Q_{d,t}^{dc})^2, \tag{3}$$

$$C_t^S = \sum_{d\in\mathcal{D}} c_d^S (S_{d,t}^{dc})^2, \tag{4}$$

$$C_t^{\text{grid}} = c_0^{(2)} P_{0,t}^2 + c_0^{(1)} P_{0,t}. \tag{5}$$

The coefficients are benchmark cost weights. All objective values are reported in cost units.

The multiple-operator formulation follows resource ownership. The regional sets form disjoint partitions,

$$\mathcal{N} = \dot{\bigcup_{r\in\mathcal{R}}} \mathcal{N}_r, \qquad \mathcal{G} = \dot{\bigcup_{r\in\mathcal{R}}} \mathcal{G}_r, \qquad \mathcal{D} = \dot{\bigcup_{r\in\mathcal{R}}} \mathcal{D}_r, \tag{6}$$

and E_r maps the system dispatch to the resources owned by operator r:

$$\boldsymbol{P}_{r,t} = E_r \boldsymbol{P}_t, \qquad C_t(\boldsymbol{P}_t) = \sum_{r \in \mathcal{R}} C_{r,t}(\boldsymbol{P}_{r,t}). \tag{7}$$

Inter-operator branches couple the nodal balances in Eq. (15), while each $C_{r,t}$ contains only the cost terms of resources in $\mathcal{G}_r$. Equations (1)–(7) define the centralized reference formulation. Section 3.3 solves the same fixed-cut problem without exchanging the complete functions $C_{r,t}$.

For receiving-end HVDC terminal $d \in \mathcal{D}$, the adopted terminal characteristic is

$$Q^{dc}_{d,t} = \kappa_d P^{dc}_{d,t}, \tag{8}$$

$$(S^{dc}_{d,t})^2 = (P^{dc}_{d,t})^2 + (Q^{dc}_{d,t})^2 = (1 + \kappa_d^2)(P^{dc}_{d,t})^2, \tag{9}$$

which leads to the effective active-power limit

$$P^{dc}_{d,t} \le \widehat{P}^{\max}_d \equiv \min \left\{ P^{\max}_d, \frac{S^{\text{rated}}_d}{\sqrt{1 + \kappa_d^2}} \right\}. \tag{10}$$

The benchmark coefficient κ_d is calibrated from the magnitude ratio $|Q^0_d|/|P^0_d|$ at the terminal operating point. Equation (10) reduces the admissible DC transfer as reactive exchange occupies converter capacity. The model also imposes a minimum transfer:

$$P^{dc}_{d,t} \ge \max \left\{ P^{\min}_d, \alpha \widehat{P}^{\max}_d \right\}, \qquad d \in \mathcal{D}, \tag{11}$$

The output floor keeps the dispatch within the operating range used to construct the dynamic equivalent. Section 4 reports the value of α.

The coordinator uses a convex master model for repeated cutting-plane and ADMM updates. Let $\widetilde{\boldsymbol{P}}_t$ denote the master dispatch. The transformer-aware branch equations follow the MATPOWER convention [25]:

$$b_{ij} = \frac{\nu_{ij}}{x_{ij} a_{ij}}, \tag{12}$$

$$F_{ij,t} = B_{\text{base}} b_{ij} \left(\theta_{i,t} - \theta_{j,t} - \varphi_{ij} \right), \qquad (i,j) \in \mathcal{L}, \tag{13}$$

$$-\overline{F}_{ij} \le F_{ij,t} \le \overline{F}_{ij}, \tag{14}$$

Here B_{base} is the system power base. The tap ratio is $a_{ij} = 1$ for an ordinary branch, and φ_{ij} is expressed in radians. For an oriented branch e, σ_{ie} equals $+1$ at the sending bus, -1 at the receiving bus, and zero elsewhere. Nodal balance requires

$$\sum_{g \in \mathcal{G}_i} P_{g,t} + P^{\text{RES}}_{i,t} - P^{\text{L}}_{i,t} = \sum_{e \in \mathcal{L}} \sigma_{ie} F_{e,t}. \tag{15}$$

The external-grid angle is fixed to zero, and all angles lie within $[-\pi, \pi]$. These equations define the convex coordination model.

For a fixed cut set $\mathcal{C}_t$, the resulting master is a convex quadratic program:

$$\min_{\widetilde{\boldsymbol{P}}_t, \boldsymbol{\theta}_t, \boldsymbol{F}_t} C_t(\widetilde{\boldsymbol{P}}_t) \quad \text{s.t.} \quad (\widetilde{\boldsymbol{P}}_t, \boldsymbol{\theta}_t, \boldsymbol{F}_t) \in \Omega_t^{\mathrm{M}} \cap \Omega_t^{\mathrm{stab}}(\mathcal{C}_t), \tag{16}$$

where Ω_t^{M} collects Eqs. (10)–(15), and Ω_t^{stab} is defined below.

After each master solve, a nonlinear network step computes the final operating point. Let $Y = G + \mathrm{j}B$ denote the bus-admittance matrix and $\theta_{ij,t} = \theta_{i,t} - \theta_{j,t}$. Active- and reactive-power balance require

$$P_{i,t}^{\mathrm{G}} + P_{i,t}^{\mathrm{RES}} - P_{i,t}^{\mathrm{L}} = V_{i,t} \sum_{j \in \mathcal{N}} V_{j,t} \left(G_{ij} \cos \theta_{ij,t} + B_{ij} \sin \theta_{ij,t} \right), \tag{17}$$

$$Q_{i,t}^{\mathrm{G}} - Q_{i,t}^{\mathrm{L}} = V_{i,t} \sum_{j \in \mathcal{N}} V_{j,t} \left(G_{ij} \sin \theta_{ij,t} - B_{ij} \cos \theta_{ij,t} \right). \tag{18}$$

The network-feasible set Ω_t^{AC} also imposes

$$\underline{V}_i \le V_{i,t} \le \overline{V}_i, \quad Q_g^{\min} \le Q_{g,t} \le Q_g^{\max}, \quad P_{ij,t}^2 + Q_{ij,t}^2 \le (\overline{S}_{ij})^2, \tag{19}$$

together with Eqs. (9) and (10). Thus, the HVDC terminal P–Q relation is enforced in both the economic model and the nonlinear AC network. The final schedule is obtained from

$$(\boldsymbol{P}_t^{\mathrm{AC}}, \boldsymbol{Q}_t^{\mathrm{AC}}, \boldsymbol{V}_t^{\mathrm{AC}}, \boldsymbol{\theta}_t^{\mathrm{AC}}) = \arg\min_{\Omega_t^{\mathrm{AC}}} \|\boldsymbol{P}_t - \widetilde{\boldsymbol{P}}_t\|_2^2 + \varepsilon_C C_t(\boldsymbol{P}_t), \tag{20}$$

where ε_C is a small economic tie breaker. This step supplies network losses and enforces reactive balance, voltage limits, generator limits, and branch ratings. It preserves the convex coordination problem while returning a network-feasible AC operating point.

3.2 Adaptive stability-constraint formulation

The AC/DC-coupled apparent-power loading of HVDC terminal d is

$$\ell_{d,t}^{dc} = \frac{\sqrt{(P_{d,t}^{dc})^2 + (Q_{d,t}^{dc})^2}}{S_d^{\mathrm{rated}}}, \tag{21}$$

and is clipped to $[0, 1]$ in the dynamic parameter map. The active-power-only comparator replaces Eq. (21) by

$$\ell_{d,t}^{P} = \frac{|P_{d,t}^{dc}|}{S_d^{\mathrm{rated}}}. \tag{22}$$

All economic terms, terminal P–Q equations, capability limits, and AC network constraints remain unchanged in that comparator. Only the dynamic representation

changes: the active-only model uses $\ell^P_{d,t}$ and removes incremental terminal coupling, whereas the proposed model uses $\ell^{dc}_{d,t}$ and $\Delta Q^{dc}_{d,t} = \kappa_d \Delta P^{dc}_{d,t}$.

The small-disturbance model is obtained from a linearized AC/DC differential–algebraic system. Let $\Delta \boldsymbol{w}_t = [\Delta \boldsymbol{\delta}_t^\top, \Delta \boldsymbol{V}_t^\top]^\top$ contain the angle and voltage states of the retained HVDC terminal buses, and let $\Delta \boldsymbol{y}_t$ contain the angle and voltage variables of the algebraic buses. The linearized active- and reactive-power equations are partitioned as

$$\begin{bmatrix} \Delta \boldsymbol{s}_{d,t} \\ \boldsymbol{0} \end{bmatrix} = \begin{bmatrix} J_{dd,t} & J_{da,t} \\ J_{ad,t} & J_{aa,t} \end{bmatrix} \begin{bmatrix} \Delta \boldsymbol{w}_t \\ \Delta \boldsymbol{y}_t \end{bmatrix}, \qquad \Delta \boldsymbol{s}_{d,t} = \begin{bmatrix} \Delta \boldsymbol{P}_{d,t} \\ \Delta \boldsymbol{Q}_{d,t} \end{bmatrix}. \tag{23}$$

The four physical sensitivity blocks $J_{P\theta,t}$, $J_{PV,t}$, $J_{Q\theta,t}$, and $J_{QV,t}$ are contained in this Jacobian. Assuming $J_{aa,t}$ is nonsingular, the algebraic variables are eliminated by a Schur complement:

$$J_{\mathrm{red},t} = J_{dd,t} - J_{da,t} J_{aa,t}^{-1} J_{ad,t} = \begin{bmatrix} J_{P\theta,t} & J_{PV,t} \\ J_{Q\theta,t} & J_{QV,t} \end{bmatrix}. \tag{24}$$

The retained terminal dynamics are

$$\Delta \dot{\boldsymbol{\delta}}_t = -M_{P,t} \Delta \boldsymbol{P}_{d,t}, \tag{25}$$

$$T_{V,t} \Delta \dot{\boldsymbol{V}}_t = -\Delta \boldsymbol{V}_t - M_{Q,t} \left(\Delta \boldsymbol{Q}_{d,t} - K_{QP} \Delta \boldsymbol{P}_{d,t} \right), \tag{26}$$

where $K_{QP} = \mathrm{diag}(\kappa_d)$. The second equation is the key AC/DC coupling channel. An active-transfer perturbation changes terminal reactive exchange and therefore changes the voltage-control mismatch. Substituting Eq. (24) into Eq. (26) gives

$$\frac{d}{dt} \begin{bmatrix} \Delta \boldsymbol{\delta}_t \\ \Delta \boldsymbol{V}_t \end{bmatrix} = A_t^V \begin{bmatrix} \Delta \boldsymbol{\delta}_t \\ \Delta \boldsymbol{V}_t \end{bmatrix}, \tag{27}$$

with

$$A_t^V = \gamma_J \begin{bmatrix} -M_{P,t} J_{P\theta,t} & -M_{P,t} J_{PV,t} \\ -T_{V,t}^{-1} M_{Q,t} (J_{Q\theta,t} - K_{QP} J_{P\theta,t}) & -\gamma_J^{-1} T_{V,t}^{-1} - T_{V,t}^{-1} M_{Q,t} (J_{QV,t} - K_{QP} J_{PV,t}) \end{bmatrix}. \tag{28}$$

Here γ_J scales the nominal network Jacobian used by the scheduling model. The operating-point maps are

$$m_{P,d,t} = m^0_{P,d} \left(1.28 - 0.18 \ell^{dc}_{d,t} - 0.22 (\ell^{dc}_{d,t})^2 \right), \tag{29}$$

$$m_{Q,d,t} = m^0_{Q,d} \left(1.20 - 0.14 \ell^{dc}_{d,t} - 0.24 (\ell^{dc}_{d,t})^2 \right), \tag{30}$$

$$\tau_{P,d,t} = \tau^0_{P,d} \left(1.08 - 0.12 \ell^{dc}_{d,t} + 0.10 (\ell^{dc}_{d,t})^2 \right), \tag{31}$$

$$\tau_{V,d,t} = \tau^0_{V,d} \left(1.05 - 0.08 \ell^{dc}_{d,t} + 0.12 (\ell^{dc}_{d,t})^2 \right). \tag{32}$$

Equations (23)–(28) define the reduced AC/DC voltage-dynamic state-space model used by the scheduler. The nonlinear loading map captures the stronger change in terminal response near high loading.

Semidefinite formulations are established tools for both control certificates and convex power-system optimization [16, 26]. For a fixed A_t^V, the Lyapunov–SDP index used here is defined by [18]

$$\eta_t(\boldsymbol{P}_t^{dc}, \boldsymbol{Q}_t^{dc}) = \min_{\Phi_t, \eta_t} \quad \eta_t \tag{33}$$

$$\text{s.t.} \quad -(A_t^V)^\top \Phi_t - \Phi_t A_t^V + \eta_t I \succeq 0, \tag{34}$$

$$\epsilon I \preceq \Phi_t \preceq I, \qquad \Phi_t = \Phi_t^\top. \tag{35}$$

A more negative η_t indicates a stronger Lyapunov certificate for the scheduling model. The threshold $\bar{\eta}^{\mathrm{M}}$ screens candidate dispatches before the nonlinear AC step. The scheduling model and the post-projection model have different state order and network linearization. Their indices are therefore not treated as interchangeable. Final acceptance uses the spectral abscissa $\alpha_t^{\mathrm{AC}} = \max \Re\{\lambda(A_t^{\mathrm{AC}})\}$ and requires $\alpha_t^{\mathrm{AC}} \leq \bar{\alpha} < 0$.

At reference master dispatch $\widetilde{\boldsymbol{P}}_t^{(q)}$, the sensitivity of the index is approximated by a central finite difference with perturbation ΔP:

$$\left[\nabla \eta_t^{(q)}\right]_g \approx \frac{\eta_t(\widetilde{\boldsymbol{P}}_t^{(q)} + \Delta P \boldsymbol{e}_g) - \eta_t(\widetilde{\boldsymbol{P}}_t^{(q)} - \Delta P \boldsymbol{e}_g)}{2\Delta P}, \tag{36}$$

with one-sided adjustment near a lower bound. The affine cut is

$$\eta_t(\widetilde{\boldsymbol{P}}_t^{(q)}) + \left(\nabla \eta_t^{(q)}\right)^\top (\widetilde{\boldsymbol{P}}_t - \widetilde{\boldsymbol{P}}_t^{(q)}) \leq \bar{\eta}^{\mathrm{M}}. \tag{37}$$

All cuts generated for period t are retained in $\mathcal{C}_t$. The finite-difference scheme approximates the local SDP-index gradient without requiring analytical dual sensitivity [19]. Because this approximation is local, the SDP index is re-evaluated at every updated dispatch [27].

The nonlinear network step can move the dispatch away from the SDP linearization point. The validation state matrix A_t^{AC} is therefore reconstructed at the updated operating point. If $\alpha_t^{\mathrm{AC}} > \bar{\alpha} + \epsilon_\alpha$, the mapping from master dispatch to the validation spectral abscissa is linearized:

$$\alpha_t^{\mathrm{AC}}(\widetilde{\boldsymbol{P}}_t^{(q)}) + \left(\nabla \alpha_t^{(q)}\right)^\top (\widetilde{\boldsymbol{P}}_t - \widetilde{\boldsymbol{P}}_t^{(q)}) \leq \bar{\alpha}. \tag{38}$$

Each component of $\nabla \alpha_t^{(q)}$ is obtained by perturbing one master output. The nonlinear network problem and AC Jacobian are then recomputed. This corrective cut is added when the validation limit is violated. Final acceptance requires

$$(\boldsymbol{P}_t^{\mathrm{AC}}, \boldsymbol{Q}_t^{\mathrm{AC}}, \boldsymbol{V}_t^{\mathrm{AC}}, \boldsymbol{\theta}_t^{\mathrm{AC}}) \in \Omega_t^{\mathrm{AC}}, \qquad \alpha_t^{\mathrm{AC}} \leq \bar{\alpha} + \epsilon_\alpha. \tag{39}$$

The single-cut comparator stops at the first affine-feasible point. The proposed procedure instead re-evaluates the SDP index at each candidate and retains every corrective cut. It also adds Eq. (38) when the validation limit is violated.

3.3 Selection-matrix-based consensus ADMM formulation

The decomposition follows operator ownership rather than an arbitrary algebraic partition. Region r controls the resources in $\mathcal{G}_r$ and evaluates its private active-transfer, reactive-support, capacity-occupation, and local generation costs. The regional proposal $\boldsymbol{x}_{r,t}$ contains only the active outputs required for coordination. The system vector $\boldsymbol{z}_t$ collects all regional outputs and the external-grid exchange. A binary matrix E_r selects the entries owned by region r.

This is a global-variable consensus relation with selection matrices. The local vectors are not required to be identical across operators; instead, each local proposal must agree with the corresponding component of the common system vector:

$$\boldsymbol{x}_{r,t} = E_r \boldsymbol{z}_t, \qquad r \in \mathcal{R}. \tag{40}$$

Thus, $\boldsymbol{z}_t$ is the system-wide consensus dispatch, while $E_r \boldsymbol{z}_t$ is the portion assigned to operator r. If a variable is shared by multiple operators, the corresponding rows of their selection matrices extract the same component of $\boldsymbol{z}_t$ and enforce agreement among their local copies.

Using the ownership and cost decomposition in Eqs. (6) and (7), each region performs the following update at ADMM iteration k:

$$\boldsymbol{x}_{r,t}^{k+1} = \arg \min_{\underline{\boldsymbol{P}}_r \le \boldsymbol{x}_r \le \overline{\boldsymbol{P}}_r} C_{r,t}(\boldsymbol{x}_r) + \frac{\rho_P}{2} \|\boldsymbol{x}_r - E_r \boldsymbol{z}_t^k + \boldsymbol{u}_{r,t}^k\|_2^2. \tag{41}$$

After substituting the P–Q relation, $C_{r,t}$ remains a diagonal quadratic cost. Equation (41) therefore has a componentwise clipped closed form. The coordinator then performs the consensus projection

$$\boldsymbol{z}_t^{k+1} = \arg \min_{\boldsymbol{z} \in \Omega_t^{\mathrm{M}} \cap \Omega_t^{\mathrm{stab}}(\mathcal{C}_t)} \frac{\rho_P}{2} \sum_{r \in \mathcal{R}} \|E_r \boldsymbol{z} - (\boldsymbol{x}_{r,t}^{k+1} + \boldsymbol{u}_{r,t}^k)\|_2^2, \tag{42}$$

where Ω_t^{M} reconstructs master nodal injections from $\boldsymbol{z}$, balances net demand, and imposes branch-transfer and external-grid limits. The set $\Omega_t^{\mathrm{stab}}(\mathcal{C}_t)$ contains every SDP and validation-model stability cut generated for the same period. Regional dual variables are updated by

$$\boldsymbol{u}_{r,t}^{k+1} = \boldsymbol{u}_{r,t}^k + \boldsymbol{x}_{r,t}^{k+1} - E_r \boldsymbol{z}_t^{k+1}. \tag{43}$$

The normalized residuals aggregate the regional disagreements:

$$r_t^k = \left(\frac{1}{|\mathcal{G}|} \sum_{r \in \mathcal{R}} \|\boldsymbol{x}_{r,t}^k - E_r \boldsymbol{z}_t^k\|_2^2 \right)^{1/2}, \tag{44}$$

$$s_t^k = \rho_P \left(\frac{1}{|\mathcal{G}|} \sum_{r \in \mathcal{R}} \| E_r(\boldsymbol{z}_t^k - \boldsymbol{z}_t^{k-1}) \|_2^2 \right)^{1/2}. \tag{45}$$

The fixed-cut problem terminates when $r_t^k \leq \epsilon_{\text{ADMM}}$ and $s_t^k \leq \epsilon_{\text{ADMM}}$. Section 4 reports ρ_P, ϵ_{ADMM}, and the iteration limit.

The complete procedure nests selection-matrix-based consensus ADMM inside posterior stability verification. For each period, the method initializes an unconstrained network dispatch, builds and accumulates SDP cuts, and solves each fixed-cut problem with Eqs. (41)–(43). It then applies the nonlinear projection in Eq. (20) and reconstructs A_t^{AC}. A violation of $\bar{\alpha}$ adds Eq. (38) and restarts the coordinated dispatch. The centralized and distributed methods use the same final cut set in the consistency comparison, which isolates the effect of the solution architecture.

The architecture is coordinator-assisted and distributed. It is designed for several operators that share declared operating bounds and system security data but retain complete local objective functions and internal scheduling records. Regional economic updates are separable for a fixed $\boldsymbol{z}_t$ and can run in parallel. The coordinator enforces the coupled network and small-disturbance stability requirements through Eqs. (42) and (20). Active-power dispatch is used as the consensus variable because the accumulated cuts act directly on active outputs. Boundary-angle agreement alone does not force the regional economic decisions to satisfy the same system-level stability boundary.

4 Case Studies

4.1 Test system and settings

The test network is based on the IEEE/New England 39-bus benchmark distributed with MATPOWER [28]. The study modifies it as a receiving-end-grid equivalent. Buses 30–38 represent nine aggregated receiving-end HVDC terminals. Their benchmark active and reactive injections calibrate the terminal P–Q ratios and ratings provided in Supplementary Note 1. Bus 39 represents the external AC grid and angle reference. Solar generation is connected at buses 15 and 16, and wind generation at buses 24 and 25. The remaining buses retain the benchmark transmission and load data.

To test coordination among multiple operators, the benchmark is assigned a constructed three-operator ownership structure that follows the conceptual architecture in Fig. 1. Operator 1 owns buses 1–14, terminals 30–32, and the external-grid equivalent at bus 39. Operator 2 owns buses 15–23 and terminals 33–36. Operator 3 owns buses 24–29 and terminals 37–38. Six branches cross operator boundaries and couple their nodal balances. This ownership assignment is a case-study assumption rather than operator information contained in the original IEEE benchmark. Figure 1 illustrates the coordination structure rather than the exact IEEE 39-bus topology; the bus-level partition is therefore specified here.

The renewable trajectories are derived from the IEEE DataPort "Hybrid Energy Forecasting and Trading Competition" dataset [29]. The study uses the wind and solar observations from 19 January 2024. Solar output is converted to a capacity factor using

the installed capacity. Wind output is normalized by its daily maximum. The hourly factors are then scaled to 450 MW of solar capacity and 750 MW of wind capacity. The load trajectory applies the following daily multiplier to the total benchmark demand: $\mathrm{clip}_{[0.72,1.08]}\{0.88+0.20\sin[2\pi(t-7)/24]+0.06\sin(4\pi t/24)\}$; bus demands retain their benchmark participation factors.

The load ranges from 4503.05 to 6754.57 MW. Solar and wind generation range from 0 to 186.20 MW and from 330.96 to 750 MW, respectively. Net load ranges from 3779.70 to 6203.14 MW. Each hour is optimized independently, giving 24 operating conditions without intertemporal coupling. The model focuses on dispatch and excludes ramping, storage state of charge, forecast uncertainty, and reserve deployment.

The test platform has an AMD Ryzen 7 5800H processor and 15.9 GB of memory. The implementation uses Python 3.12.2, CVXPY 1.9.0, NumPy 2.4.3, pandas 3.0.1, and PYPOWER [30]. CLARABEL and OSQP solve the convex subproblems. PYPOWER solves Eq. (20) with a primal–dual interior-point method. The system base is $B_{\mathrm{base}} = 100$ MVA. Emergency branch limits are set to twice the static MATPOWER ratings for this benchmark. The remaining settings are $\gamma_J = 0.18$, $\Delta P = 5$ MW, $\varepsilon_C = 10^{-5}$, $\alpha = 0.15$, $\rho_P = 0.2$, and $\epsilon_{\mathrm{ADMM}} = 10^{-3}$. The algorithm allows 100 ADMM iterations, 24 SDP cuts, and four operating-point corrective cuts per period.

The scheduling target is $\bar{\eta}^{\mathrm{M}} = -0.0703$. Final acceptance uses $\bar{\alpha} = -0.120\ \mathrm{s}^{-1}$ for the independently reconstructed AC voltage-dynamic model. The two limits were fixed after a preliminary feasible-boundary sweep and are used unchanged in every comparison. They serve different models and are not interpreted as numerically equivalent. The final limit corresponds to a 5% exponential envelope time of approximately 25.0 s.

4.2 Overall operation and stability performance

This subsection first evaluates the daily economic–stability tradeoff and then checks the final operating points against the nonlinear AC network model. Table 1 and Fig. 3 compare the baseline OPF with the stability-constrained solution. Both use the same steady-state AC/DC model. The baseline violates the prescribed voltage-dynamic margin in three periods. Its worst validation spectral abscissa is $-0.115554\ \mathrm{s}^{-1}$. The proposed method satisfies the limit in all periods, with a worst value of $-0.120494\ \mathrm{s}^{-1}$.

The small-disturbance stability requirement raises total cost by 4,180 cost units, or 0.123%. Active-transfer cost increases by 4,793 units, while external-grid cost decreases by 1,602 units. Reactive-support and capacity-occupation costs rise by 170 and 819 units. The mean validation spectral abscissa changes from -0.13875 to $-0.13945\ \mathrm{s}^{-1}$. The largest hourly improvement is $4.99 \times 10^{-3}\ \mathrm{s}^{-1}$. The redispatch is concentrated in periods close to the prescribed voltage-dynamic boundary.

The nonlinear network rows in Table 1 cover active losses, reactive balance, voltage magnitudes, generator reactive-power limits, P–Q equalities, apparent-capacity limits, and branch ratings.

Both schedules satisfy all network constraints in every period. The largest HVDC terminal P–Q equality error remains at numerical precision. Stability-constrained redispatch reduces mean network loss by 0.10 MW. Maximum branch loading

Table 1 Baseline and stability-constrained results over 24 hourly periods

Metric	Baseline OPF	Stability-constrained OPF
Total cost	3,411,631.20	3,415,811.61
Active-power cost	2,014,024.56	2,018,817.88
Reactive-support cost	44,385.57	44,555.69
Apparent-capacity cost	323,288.56	324,107.93
External-grid cost	1,029,932.52	1,028,330.11
Worst scheduling SDP index η	-0.068560	-0.068966
Worst validation spectral abscissa (s^{-1})	-0.115554	-0.120494
Periods satisfying the small-disturbance limit	21/24	24/24
Network-feasible periods	24/24	24/24
Periods satisfying all nonlinear AC limits	24/24	24/24
Voltage range (p.u.)	0.9400–1.0600	0.9400–1.0600
Maximum branch apparent-power loading	0.7408	0.7491
Maximum HVDC-terminal apparent-power loading	0.9657	0.9152
Mean network loss (MW)	51.86	51.76
Maximum terminal P–Q error (MVAr)	5.7×10^{-14}	5.7×10^{-14}

rises from 0.7408 to 0.7491 while remaining within its limit. The voltage-dynamic improvement therefore does not create a steady-state network violation.

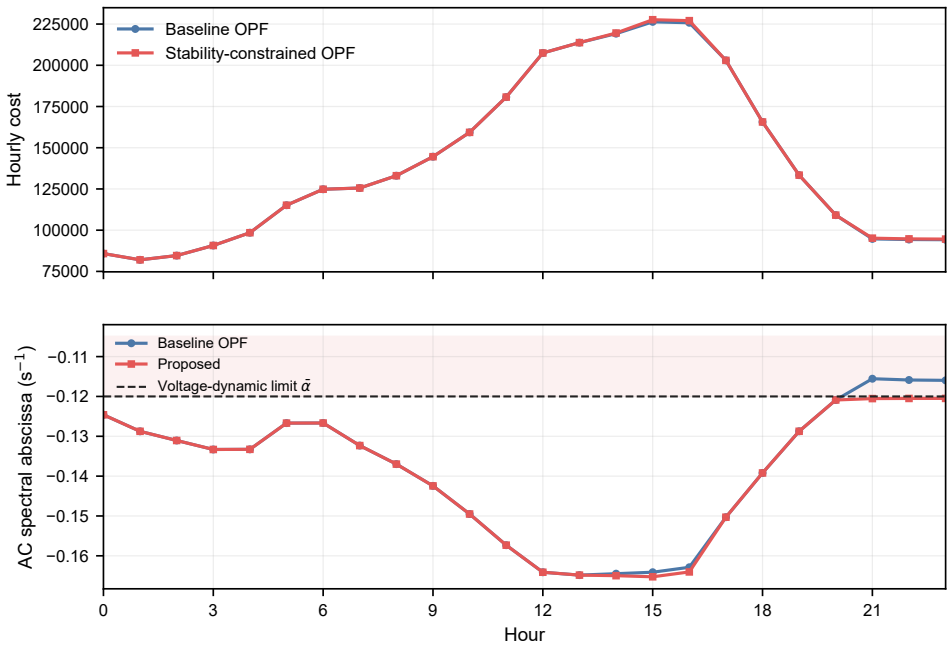

Fig. 3 Hourly operating cost and validation-model spectral abscissa. The dashed line is the prescribed voltage-dynamic limit $\bar{\alpha} = -0.120\ \mathrm{s}^{-1}$.

4.3 Comparative studies of the three contributions

Three controlled comparisons isolate the effects of the AC/DC-coupled HVDC model, the adaptive stability cuts, and the selection-matrix-based consensus ADMM. All candidate schedules are evaluated using the same nonlinear AC network model and independent dynamic check. Each comparison changes only the modeling or solution component under investigation.

4.3.1 AC/DC-coupled HVDC terminal loading

This comparison changes only the dynamic stability representation. The proposed model uses $\ell^{dc}_{d,t}$ and K_{QP} in Eqs. (28)–(32). The active-power-only model uses $\ell^{P}_{d,t}$ and omits the incremental P–Q coupling from the voltage-dynamic matrix. Both models retain the same objective, steady-state relation $Q^{dc}_{d,t} = \kappa_d P^{dc}_{d,t}$, apparent-power rating, active-transfer limits, and nonlinear AC network constraints. The resulting schedules are then assessed with the full coupled model and the independent AC-Jacobian model.

Table 2 Effect of AC/DC-coupled HVDC terminal dynamics

Metric	Active-power-only	Proposed coupled model
Total cost	3,411,631	3,415,812
Independent-check-compliant periods	21/24	24/24
False-feasible SDP classifications	1	0
Maximum terminal apparent loading	0.9657	0.9152

Table 2 shows that the active-power-only model reduces the 24-hour cost by 0.122%, but changes the dispatch by 658.16 MWh in cumulative absolute output. Restoring K_{QP} at the same dispatch changes one SDP classification from feasible to infeasible. The independent voltage-dynamic check rejects three periods, whereas the proposed coupled model passes all 24 periods. The lower maximum apparent loading also indicates that the coupled model preserves more terminal capacity for reactive exchange. These results show that terminal reactive-power response affects both the stability classification and the operating schedule, even when the steady-state AC equations enforce the P–Q relation.

4.3.2 Adaptive stability cuts

The second comparison isolates the role of posterior verification. Both methods start from the same OPF and use a 5 MW finite-difference step. The single-cut method solves one affine-constrained OPF for each period and accepts the resulting candidate. The proposed method recomputes the SDP index and nonlinear AC operating point, retains previous cuts, and adds a corrective cut whenever the candidate violates the final stability check.

Table 3 Comparison of single-cut and adaptive stability-cut methods

Metric	Single cut	Proposed adaptive cuts
Total cost	3,414,113	3,415,812
Posterior-compliant periods	19/24	24/24
False-feasible periods	5	0
Total cuts / master solves	24 / 48	30 / 54
Nonlinear AC solves	24	57
Total wall-clock time (s)	90.51	110.22

All 24 candidates from the single-cut method satisfy their local affine constraints, but five fail after the SDP index and nonlinear operating point are recomputed. The largest underestimation of η is 0.001364. The adaptive method adds six corrective cuts and removes all five false-feasible periods. The final cost increases by 0.050% relative to the single-cut result. The additional posterior checks increase the wall-clock time by 19.71 s, or 21.8%, while ensuring that every final operating point satisfies both the network constraints and the independent small-disturbance limit. This comparison

demonstrates the value of cumulative correction when a candidate moves beyond the reliable neighborhood of its initial affine approximation.

4.3.3 Selection-matrix-based consensus ADMM coordination

The centralized reference pools all regional objective functions and solves the verified cut set and network model as one optimization problem. The distributed method uses the same model and final cut set, but each operator retains its complete local objective function and internal scheduling record. Panel A of Table 4 compares their 24-hour solutions.

Table 4 Distributed coordination performance and consensus-variable ablation

Panel A. Centralized and distributed consistency over 24 hourly periods		
Metric	Centralized	Distributed
Total cost	3,415,811.61	3,415,811.64
Maximum dispatch difference (MW)	–	0.00085
Maximum relative period-cost difference	–	4.78×10^{-8}
Maximum spectral-abscissa difference (s^{-1})	–	2.73×10^{-8}
Maximum primal / dual residual	–	9.44×10^{-4} / 7.22×10^{-5}
Mean / maximum ADMM iterations	–	18.38 / 19
Panel B. Consensus-variable ablation over three representative periods		
Metric	Active-power consensus	Boundary-angle consensus
Converged periods	3/3	0/3
Physically feasible periods	3/3	0/3
Maximum dispatch error (MW)	0.00062	31.17
Maximum power-balance residual (MW)	1.82×10^{-12}	63.28
Mean / maximum iterations	18.67 / 19	100 / 100

The proposed ADMM converges in every period within 19 iterations. Its largest dispatch difference from the centralized solution is 0.00085 MW, and its maximum relative period-cost difference is 4.78×10^{-8}. The validation spectral abscissa also agrees within 2.73×10^{-8} s^{-1}. The two solution architectures therefore produce numerically consistent schedules under the stated stopping and solver tolerances, while the distributed implementation avoids collecting complete regional objective functions and internal scheduling records.

The second comparison isolates the effect of the consensus variable. Both variants retain regional subproblems and use the same three representative periods. The proposed selection matrix extracts generator active-power decisions for coordination, whereas the comparator exchanges duplicated boundary voltage angles. Panel B of Table 4 reports the results.

Active-power consensus converges in all three periods and yields physically feasible schedules. Its maximum dispatch error is 0.00062 MW, and its power-balance residual remains at numerical precision. Boundary-angle consensus reaches the 100-iteration limit in every tested period; none of its three schedules passes the complete physical-feasibility check, and its maximum power-balance residual is 63.28 MW. This result does not imply that boundary-angle consensus is unsuitable for distributed OPF in general. It shows that active-power consensus is better aligned with the present formulation because the accumulated stability cuts act directly on generator active outputs.

4.4 Dynamic validation and parameter sensitivity

A post-projection AC-Jacobian model provides the final voltage-dynamic check. At each nonlinear AC operating point, the four Jacobian blocks $J^{\mathrm{AC}}_{P\theta,t}$, $J^{\mathrm{AC}}_{PV,t}$, $J^{\mathrm{AC}}_{Q\theta,t}$, and $J^{\mathrm{AC}}_{QV,t}$ are evaluated at the converged complex voltage. Bus 39 is the angle reference. The nonterminal angles and voltages are eliminated by a Schur complement:

$$J^{\mathrm{AC}}_{\mathrm{red},t} = J^{\mathrm{AC}}_{dd,t} - J^{\mathrm{AC}}_{da,t}(J^{\mathrm{AC}}_{aa,t})^{-1}J^{\mathrm{AC}}_{ad,t}. \tag{46}$$

The matrix $J^{\mathrm{AC}}_{\mathrm{red},t}$ varies with the voltage magnitude and angle of each schedule. It is computed independently from the nominal Jacobian used in Eq. (28).

The validation model adds measured-power and actuator-output states. Let $\Delta\boldsymbol{p}_{m,t}$ and $\Delta\boldsymbol{v}^a_t$ denote these states. The model is

$$\frac{d}{dt}\begin{bmatrix}\Delta\boldsymbol{\delta}_t\\ \Delta\boldsymbol{p}_{m,t}\\ \Delta\boldsymbol{v}^a_t\\ \Delta\boldsymbol{V}_t\end{bmatrix} = A^{\mathrm{AC}}_t\begin{bmatrix}\Delta\boldsymbol{\delta}_t\\ \Delta\boldsymbol{p}_{m,t}\\ \Delta\boldsymbol{v}^a_t\\ \Delta\boldsymbol{V}_t\end{bmatrix}, \quad A^{\mathrm{AC}}_t = \begin{bmatrix} 0 & 0 & -M_{P,t} & 0\\ T^{-1}_{P,t}J^{\mathrm{AC}}_{P\theta,t} & -T^{-1}_{P,t} & 0 & T^{-1}_{P,t}J^{\mathrm{AC}}_{PV,t}\\ 0 & (T^a)^{-1} & -(T^a)^{-1} & 0\\ -T^{-1}_{V,t}M_{Q,t}\widehat{J}^{\mathrm{AC}}_{Q\theta,t} & 0 & 0 & -T^{-1}_{V,t}\left(I + M_{Q,t}\widehat{J}^{\mathrm{AC}}_{QV,t}\right)\end{bmatrix}. \tag{47}$$

Here $\widehat{J}^{\mathrm{AC}}_{Q\theta,t} = J^{\mathrm{AC}}_{Q\theta,t} - K_{QP}J^{\mathrm{AC}}_{P\theta,t}$, $\widehat{J}^{\mathrm{AC}}_{QV,t} = J^{\mathrm{AC}}_{QV,t} - K_{QP}J^{\mathrm{AC}}_{PV,t}$, and $T^a = \mathrm{diag}(\tau^a_g)$. The validation model has 36 states, while the scheduling model has 18. The nominal actuator lag is 0.05 s. Each period also uses 50 paired parameter samples. Control and filter multipliers vary within $[0.8, 1.2]$, and actuator lag varies from 0.02 to 0.10 s. Each sample is applied to both schedules. Representative responses apply the same angle and voltage disturbance at bus 34.

The scheduling index and the validation spectral abscissa are not globally interchangeable because they use different network operating points and state orders. Across the full daily profile, their Pearson coefficient is -0.919. This result supports the two-level design: the SDP index supplies a local optimization direction, while Eq. (38) enforces the final operating-point criterion. The proposed schedule improves the worst nominal spectral abscissa by 4.94×10^{-3} s^{-1}. All 1200 parameter samples remain asymptotically stable. The proposed schedule shifts the 95th-percentile sampled abscissa from -0.11187 to -0.11502 s^{-1}. Detailed statistics for all hourly operating points and paired parameter samples are provided in Supplementary Table S1.

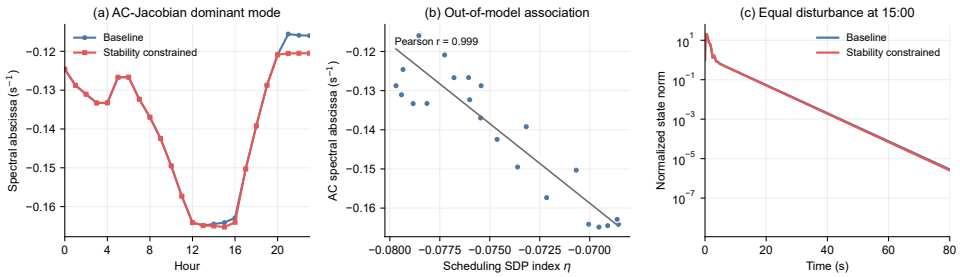

Fig. 4 Dynamic validation: (a) hourly validation spectral abscissa, (b) relation between the scheduling SDP index and the validation spectral abscissa, and (c) responses to the same disturbance at 15:00.

4.5 Discussion and limitations

Across the comparisons, the AC/DC-coupled DAE corrects small-disturbance stability classifications missed by the active-only dynamic model. Adaptive cuts correct candidates that pass a local approximation but fail operating-point re-evaluation. Selection-matrix-based consensus ADMM satisfies the shared network and stability requirements while complete regional objective functions and internal scheduling records remain local; the centralized reference confirms numerical consistency. The network and dynamic checks show that the final schedules satisfy the modeled operating constraints and prescribed voltage-dynamic margin.

The present formulation uses a convex master problem followed by nonlinear AC network projection. HVDC terminal reactive exchange follows a fixed P–Q characteristic, while practical stations may use voltage-dependent control, reactive compensation switching, and mode changes. Both dynamic models are reduced electromechanical voltage representations rather than electromagnetic-transient converter models. The coordinator receives dispatch proposals and declared operating bounds and retains the shared network and stability model. The architecture therefore limits regional information exchange but is not fully decentralized and does not provide cryptographic privacy. The case study covers one deterministic network, a constructed three-operator ownership structure, and 24 independent operating conditions.

5 Conclusion

This paper developed a distributed stability-constrained operation method for receiving-end grids with multiple operators and multiple HVDC infeeds. A linearized AC/DC DAE captures how coupled terminal active and reactive powers change converter loading, network sensitivities, and receiving-end voltage dynamics. Posterior-verified SDP cuts connect this implicit stability requirement to dispatch and correct candidates that fail operating-point verification. Selection-matrix-based consensus ADMM coordinates regional decisions under shared network and stability constraints without collecting complete local objective functions or internal scheduling records. In the constructed three-operator case derived from the IEEE 39-bus benchmark, the method eliminates the 12.5% hourly stability-violation rate at a 0.12% cost increase,

rejects all five false-feasible single-cut solutions, and converges within 19 iterations to schedules numerically consistent with the centralized optimum.

Future work will replace the fixed terminal P–Q characteristic with detailed HVDC control modes, reactive compensation, and higher-fidelity converter dynamics. Uncertainty, contingencies, intertemporal flexibility, communication delay, and larger multi-operator systems will extend the physical and computational assessment.

Declarations

Author contribution. Xiaobo Wang: Conceptualization, Methodology, Software, Validation, Writing – original draft. Haifeng Li: Conceptualization, Supervision, Project administration, Writing – review and editing. Zhe Chen: Data curation, Formal analysis, Validation, Visualization. Tao Jin: Methodology, Investigation, Validation. Mingshen Wang: Software, Data curation, Visualization.

Funding. This work is funded by the Science and Technology Project of State Grid Jiangsu Electric Power Co., Ltd., "Research on Self-Optimizing Improvement Methods for Voltage-Stability Margin in Receiving-End Power Grids Based on Swarm-Intelligence-Integrated Perception," Project Number J2025099.

Ethics approval and consent to participate. Not applicable. This study uses computational power-system models and publicly available benchmark and renewable-energy data; it does not involve human participants, animals, or human samples.

Consent for publication. Not applicable.

Data availability. The IEEE 39-bus benchmark data used in this study are publicly available through MATPOWER. The renewable profiles are derived from the IEEE DataPort "Hybrid Energy Forecasting and Trading Competition" dataset under the terms of its original license. Processed operating data and complete numerical results are available from the corresponding author upon reasonable request. Redistribution of source data remains subject to the licenses of the original providers.

Materials availability. Not applicable. This computational study does not use physical materials or biological specimens.

Code availability. The source code used for optimization, posterior verification, distributed coordination, and result analysis is provided in the accompanying reproducibility package. The package also includes a pinned environment specification, automated tests, execution instructions, and scripts for reproducing the principal results, and will be made available with the published article.

Competing interests. The authors declare that they have no known competing financial interests or personal relationships that could have appeared to influence the work reported in this paper.

Generative AI and AI-assisted technologies. During manuscript preparation, the authors used OpenAI Codex to assist with language editing, structural revision, and LaTeX formatting. The authors reviewed and edited the resulting text and take full responsibility for the content of the article.

References

[1] Kroposki, B. *et al.* Achieving a 100% renewable grid: Operating electric power systems with extremely high levels of variable renewable energy. *IEEE Power and Energy Magazine* **15**, 61–73 (2017).

[2] Kundur, P. *Power System Stability and Control* (McGraw-Hill, New York, NY, USA, 1994).

[3] Hatziargyriou, N. *et al.* Definition and classification of power system stability—revisited and extended. *IEEE Transactions on Power Systems* **36**, 3271–3281 (2021).

[4] Tielens, P. & Hertem, D. V. The relevance of inertia in power systems. *Renewable and Sustainable Energy Reviews* **55**, 999–1009 (2016).

[5] Milano, F., Dörfler, F., Hug, G., Hill, D. J. & Verbič, G. Foundations and challenges of low-inertia systems (2018). Paper presented at the 20th Power Systems Computation Conference, Dublin, Ireland.

[6] Shuai, Z. *et al.* Microgrid stability: Classification and a review. *Renewable and Sustainable Energy Reviews* **58**, 167–179 (2016).

[7] Farrokhabadi, M. *et al.* Microgrid stability definitions, analysis, and examples. *IEEE Transactions on Power Systems* **35**, 13–29 (2020).

[8] Zhang, F., Xin, H., Wu, D., Wang, Z. & Gan, D. Assessing strength of multi-infeed LCC-HVDC systems using generalized short-circuit ratio. *IEEE Transactions on Power Systems* **34**, 467–480 (2019).

[9] Luo, J., Teng, F. & Bu, S. Stability-constrained power system scheduling: A review. *IEEE Access* **8**, 219331–219343 (2020).

[10] Zarate-Minano, R., Cutsem, T. V., Milano, F. & Conejo, A. J. Securing transient stability using time-domain simulations within an optimal power flow. *IEEE Transactions on Power Systems* **25**, 243–253 (2010).

[11] Zarate-Minano, R., Milano, F. & Conejo, A. J. An OPF methodology to ensure small-signal stability. *IEEE Transactions on Power Systems* **26**, 1050–1061 (2011).

[12] Li, P. *et al.* An SQP method combined with gradient sampling for small-signal stability constrained OPF. *IEEE Transactions on Power Systems* **32**, 2372–2381 (2017).

[13] Pareek, P. & Nguyen, H. D. A convexification approach for small-signal stability constrained optimal power flow. *IEEE Transactions on Control of Network Systems* **8**, 1930–1941 (2021).

[14] Huang, Z. *et al.* Modeling of small-signal stability margin constrained optimal power flow. *International Journal of Electrical Power and Energy Systems* **162**, 110338 (2024).

[15] Liu, J. *et al.* Explicit data-driven small-signal stability constrained optimal power flow. *IEEE Transactions on Power Systems* **37**, 3726–3737 (2022).

[16] Boyd, S., Ghaoui, L. E., Feron, E. & Balakrishnan, V. *Linear Matrix Inequalities in System and Control Theory* (SIAM, Philadelphia, PA, USA, 1994).

[17] Pullaguram, D., Madani, R., Altun, T. & Davoudi, A. Small-signal stability-constrained optimal power flow for inverter dominant autonomous microgrids. *IEEE Transactions on Industrial Electronics* **69**, 7318–7328 (2022).

[18] Wang, J., Fan, F., Song, Y., Hou, Y. & Hill, D. J. Stability constrained optimal operation of inverter-dominant microgrids: A two stage robust optimization framework. *IEEE Transactions on Sustainable Energy* **15**, 1900–1913 (2024).

[19] Wang, J., Song, Y., Hill, D. J. & Hou, Y. An analytical formula for small signal stability sensitivity using SDP dual. *IEEE Transactions on Power Systems* **39**, 2345–2348 (2024).

[20] Dall'Anese, E., Zhu, H. & Giannakis, G. B. Distributed optimal power flow for smart microgrids. *IEEE Transactions on Smart Grid* **4**, 1464–1475 (2013).

[21] Erseghe, T. Distributed optimal power flow using ADMM. *IEEE Transactions on Power Systems* **29**, 2370–2380 (2014).

[22] Molzahn, D. K. *et al.* A survey of distributed optimization and control algorithms for electric power systems. *IEEE Transactions on Smart Grid* **8**, 2941–2962 (2017).

[23] Boyd, S., Parikh, N., Chu, E., Peleato, B. & Eckstein, J. Distributed optimization and statistical learning via the alternating direction method of multipliers. *Foundations and Trends in Machine Learning* **3**, 1–122 (2011).

[24] Song, Y., Hill, D. J., Liu, T. & Zheng, Y. A distributed framework for stability evaluation and enhancement of inverter-based microgrids. *IEEE Transactions on Smart Grid* **8**, 3020–3034 (2017).

[25] Stott, B., Jardim, J. & Alsac, O. DC power flow revisited. *IEEE Transactions on Power Systems* **24**, 1290–1300 (2009).

[26] Lavaei, J. & Low, S. H. Zero duality gap in optimal power flow problem. *IEEE Transactions on Power Systems* **27**, 92–107 (2012).

[27] Kelley, J. E., Jr. The cutting-plane method for solving convex programs. *Journal of the Society for Industrial and Applied Mathematics* **8**, 703–712 (1960).

[28] Zimmerman, R. D., Murillo-Sanchez, C. E. & Thomas, R. J. MATPOWER: Steady-state operations, planning, and analysis tools for power systems research and education. *IEEE Transactions on Power Systems* **26**, 12–19 (2011).

[29] Browell, J. *et al.* Hybrid energy forecasting and trading competition (2023). URL https://doi.org/10.21227/5hn0-8091. Dataset.

[30] Diamond, S. & Boyd, S. CVXPY: A python-embedded modeling language for convex optimization. *Journal of Machine Learning Research* **17**, 1–5 (2016). URL https://jmlr.org/papers/v17/15-408.html.

Supplementary Files

This is a list of supplementary files associated with this preprint. Click to download.

- scientificreportsstabilityadmmsupplementaryinformation.pdf